JOURNAL OF AIRCRAFT
Vol. 44, No. 1, January–February 2007

Comparison of Reynolds-Averaged Navier–Stokes Simulations of Multi-Element High-Lift Configurations

Mitsuhiro Murayama,* Taro Imamura,* and Kazuomi Yamamoto†
Japan Aerospace Exploration Agency, Tokyo 182-8522, Japan
and
Kunihiko Kobayashi‡
Ryoyu Systems Company, Ltd., Tokyo 108-0074, Japan

DOI: 10.2514/1.22838

In this study, flow computations are performed on three-dimensional high-lift configurations on multiblock structured and unstructured meshes with two turbulence models, Spalart–Allmaras model and Menter's shear stress transport model. Two kinds of three-element trapezoidal wings with full-span flap or part-span flap are computed. The objectives of this paper are to investigate the mesh dependency and the effect of turbulence models and improve the reliability in simulating the flow around high-lift devices. Importance of the mesh resolution to resolve the separated corner flows near the wing–fuselage junction is shown to improve the accuracy of computational results. It is also shown that the maximum lift and the angle at which it occurs are very sensitive to turbulence model and Menter's model gives better results at a higher angle of attack in the present computations.

Nomenclature

AR	=	aspect ratio of the wing
C_D	=	drag coefficient
C_{Df}	=	friction drag coefficient
C_{Dp}	=	pressure drag coefficient
$C_{D\text{profile estimated}}$	=	estimated profile drag coefficient
C_f	=	skin friction coefficient
C_L	=	lift coefficient
$C_{L\max}$	=	maximum lift coefficient
C_p	=	surface pressure coefficient
c	=	mean aerodynamic chord
e	=	Oswald efficiency factor
M_∞	=	freestream Mach number
Re	=	Reynolds number
α	=	angle of attack

I. Introduction

DEVELOPMENT of efficient high-lift devices has a strong impact of the operating cost and environments around airports, such as improvements of payload, fuel consumption, and noise emission [1]. Recent developments in CFD solving Reynolds-averaged Navier–Stokes (RANS) equations and in computers have led to high expectations of performance improvement. High-lift devices are commonly composed of leading-edge slats and trailing-edge flaps to increase lift performance in takeoff and landing. The multi-element wing system with small gaps complicates mesh generation and flow features. Flow is complicated due to boundary layer transition, flow separation, and interaction of wake of each element and boundary layer. Precise prediction of the aerodynamic forces for such complicated flow fields is required to design a high-lift system.

Recently, efforts to validate and improve CFD have been promoted for high-lift systems [2]. In the European EUROLIFT project [3], development of aerodynamic analysis for high-lift system has been intensively conducted in conjunction with experiments. Validation studies have been conducted for a two-dimensional configuration, a simplified three-dimensional configuration, and a realistic aircraft configuration. In NASA Langley, a series of simplified three-element trapezoidal high-lift wings with body pod have been tested and the experimental data are provided for validation and development of CFD methods for three-dimensional high-lift flows [4–7].§ In the Civil Transport Team of the Japan Aerospace Exploration Agency, wind-tunnel tests using a realistic aircraft takeoff and landing configuration deploying the high-lift devices with fuselage, nacelle–pylon and flap track fairing will be conducted to increase the knowledge of high-lift flows over a realistic aircraft configuration, to improve the measurement technologies, and to provide the detailed and systematic experimental data that can be disclosed for CFD validation from 2005 to 2006.

Wind-tunnel data often have large wall-interference corrections, especially for high-lift flows [6]. To validate and develop CFD methods, detailed comparison of computational results from several CFD codes and mesh topologies is helpful. We have conducted several flow computations for two- and three-dimensional high-lift configurations [8–10]. In [8–10], computations were performed using several CFD codes based on different mesh system (multiblock structured and unstructured mesh) to validate the results. Multiblock structured mesh CFD has the advantage of low computational costs and high solution accuracy. However, it requires a considerable amount of time to generate. On the other hand, an unstructured mesh method has the capability to handle the complicated configurations associated with high-lift devices in a much shorter time. In addition, it is much easier to modify the mesh when the geometry changes due to optimization study or when adaptive mesh refinement is employed [11,12]. Therefore, it is hoped that the applicability and reliability in computing high-lift flows on unstructured mesh CFD is confirmed by improving cost and accuracy.

In our previous studies [8–10], computations of two-dimensional two-element and three-element airfoils and two kinds of three-

Presented as Paper 1396 at the 44th AIAA Aerospace Sciences Meeting and Exhibit, Reno Nevada, 9–12 January 2006; received 30 January 2006; revision received 14 April 2006; accepted for publication 18 May 2006.

*Researcher, Civil Transport Team, Aviation Program Group, 7-44-1 Jindaiji-Higashi, Chofu. Member AIAA.
†Section Leader, Civil Transport Team, Aviation Program Group, 7-44-1 Jindaiji-Higashi, Chofu. Member AIAA.
‡Engineer, Engineering Solution Division, 2-19-13, Takanawa, Minato-ku.

§Data available online at http://db-www.larc.nasa.gov/trapwing/archive/register [cited 30 December 2005].

dimensional three-element trapezoidal wing models with body pod were performed. In two-dimensional problems, detailed grid studies with a mesh adaptation method on unstructured mesh [10] were performed. The dependency on the turbulence models applied to high-lift flow has been also investigated in two-dimensional computations [8,9]. Spalart–Allmaras's (SA) one-equation model [13] and Menter's shear stress transport (SST) two-equation model [14] produced similar aerodynamic forces before stall. At higher angle of attack, the SST model gave better results for the maximum lift $C_{l\max}$ and the stall angle in the computations. In the three-dimensional problems, some modest grid studies were performed with structured meshes. Aerodynamic forces were predicted reasonably even on the unstructured mesh when moderate settings of slat and flap were used. However, the difference in mesh resolution led to the difference of local flow physics. At a higher angle of attack, the difference between the results on structured and unstructured meshes became larger. In addition, results were discussed using a turbulence model, the SA model, in the previous three-dimensional studies [10]. The dependencies on the mesh density and turbulence model as applied to three-dimensional high-lift flows around multi-element configurations must be investigated, methodically.

The objectives of this study are to compare and assess structured and unstructured mesh CFD codes, investigate mesh dependency and the effect of turbulence models, and increase the knowledge in simulating the flow around high-lift devices. Especially in three-dimensional computations, fewer comparisons between structured and unstructured mesh CFD due to complexity and high computational costs. In this paper, RANS computations of three-dimensional high-lift configurations are performed using two kinds of turbulence models, the SA model and the SST model. Although prediction accuracy of boundary layer transition has a relatively large effect on computational results [15,16], we do not intend to validate transition models in this paper. The following two kinds of simplified high-lift configurations tested at NASA Langley in 1998 are computed both on multiblock structured mesh and unstructured meshes: 1) full-span flap model: three-dimensional three-element (full-span slat, main, and full-span flap) trapezoidal wing with a body pod; 2) part-span flap model: three-dimensional three-element (full-span slat, main, and part-span flap) trapezoidal wing with a body pod. First, the results of a structured mesh CFD code and an unstructured mesh CFD code using the same turbulence model, the SA model, are discussed. Next, two turbulence modes are compared using an unstructured mesh CFD code. By comparison with the results, ways to improve the reliability on structured and unstructured meshes are discussed.

II. Flow Solvers

As the flow solver on multiblock structured meshes, unified platform for aerospace computational simulation (UPACS) is used, which is a standard CFD code in the Institute of Space Technology and Aeronautics of Japan Aerospace Exploration Agency [17,18]. The flow solver is based on a cell-centered finite volume method. In this study, the third-order scheme of Roe's flux difference splitting for convection terms is used. Time integration is carried out using the matrix free Gauss–Seidel (MFGS) implicit method [19]. Multiblock structured meshes are generated with commercial software, Gridgen.

As the unstructured mesh generator and flow solver, Tohoku University aerodynamic simulation (TAS) codes [20] are used in this study. TAS-Mesh is a mesh generator with graphical user interface tools [21–24]. It can generates triangular surface mesh with the advancing front method [21,22] and tetrahedral volume mesh using Delaunay tetrahedral meshing [23], as well as hybrid volume mesh composed of tetrahedrons, prisms, and pyramids for viscous flows with high Reynolds number [24]. The unstructured surface meshing using isotropic triangles is semiautomatic and the volume mesh generation is fully automated. In TAS-Flow, Navier–Stokes equations are solved on the unstructured mesh by a cell-vertex finite volume method. The Harten–Lax–van Leer–Einfeldt–Wada (HLLEW) method [25] is used for the numerical flux computations. Second-order spatial accuracy is realized by a linear reconstruction of the primitive variables. The lower/upper symmetric Gauss–Seidel (LU-SGS) implicit method [26] is used for time integration.

In this study, two turbulence models, the SA one-equation model [13] and Menter's SST two-equation model [14], have been used to simulate turbulent flows. In the study, the SA model is used as a standard model.

Both UPACS and TAS employed the SA model without the trip term for transition and the $ft2$ function, which tend to suppress production of eddy viscosity due to numerical error. The production of eddy viscosity starts with the free stream value. A variation of the model, which reduces the eddy viscosity in the regions of high vorticity [27,28], is also used. In this study, a simple combination using the minimum of the vorticity $\Omega = \sqrt{2\Omega_{ij}\Omega_{ij}}$ and strain rate $\hat{S} = \sqrt{2s_{ij}s_{ij}}$ is usd in the modification [28] as follows:

$$S = \Omega + C_{\text{vor}} \min(0, \hat{S} - \Omega) \tag{1}$$

Here, $C_{\text{vor}} = 1$ for the present computations. The modified model computes turbulent vortical flow without adding much dissipation to the vortex core.

Menter's SST model combined the k–ε and k–ω models in a way that would allow them to be used in the regions where they achieve the best advantage. The model uses the k–ω model near wall, and switches to k–ε model away from the wall. Furthermore, the model limits the shear stress, based on experimental observation to improve the results in separated flows. In this study, the following modification is used in the production terms:

$$\tau_{ij}\frac{\partial u_i}{\partial xj} \cong \mu_T \Omega^2 \tag{2}$$

Computations were carried out on a Fujitsu PRIMEPOWER HPC2500 multiprocessor, which is the main machine of the Numerical Simulator III system in the Japan Aerospace Exploration Agency [29]. Although computational times varied depending on the number of CPUs, the mesh size, and the angle of attack, solutions results required about 1–3 days per angle of attack using 100 processors to reach convergence. Typically, 50 or 100 CPUs were used for each computation.

III. Model Geometry and Computational Conditions

Two kinds of trapezoidal high-lift wing models [4][‖] were computed both on multiblock structured and unstructured meshes, as shown in Figs. 1–4. One is a full-span flap model that has a full-span slat and a full-span single-slotted flap that extend from wing root to wing tip. The other is a part-span flap model that has a full-span slat and a part-span flap that has a span equal to roughly half of the span length of the model. The models are semispan models. They were tested at the NASA Langley Research Center 14 by 12 ft subsonic wind tunnel and the NASA Ames Research Center 12 ft pressure wind tunnel (PWT). The experiments using the models were performed to produce experimental data for validation and development of CFD methods for three-dimensional high-lift flows [4].[¶] In the wind-tunnel tests, the models have a variety of slat and flap settings. In this study, a setting for landing is used for both configurations. The slat and flap deflections are 30 and 25 deg, respectively. The model semispan is 85.1 in. and c is 39.6 in. AR is 4.56. The slat gap and slat height are $0.015c$. The flap gap and flap overlap are $0.015c$ and $0.005c$, respectively. In this study, the experimental data at the NASA Ames PWT are compared with the computational results. The test section has a 12 ft diameter circular cross section with four 4 ft-wide flat surfaces centered about the horizontal and vertical centerlines. The width and height of the test section is 11.3 ft, and the length is 28 ft. A splitter plate is installed in the test section for semispan testing. The plate is 19 ft long and

[‖]See http://db-www.larc.nasa.gov/trapwing/archive/register [cited 30 December 2005].

[¶]See http://db-www.larc.nasa.gov/trapwing/archive/register [cited 30 December 2005].

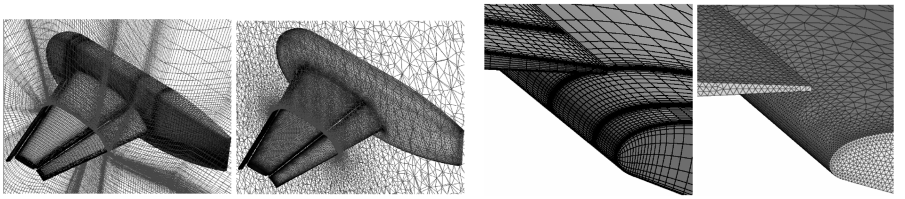

a) Distant view b) Close-up view near leading edge of flap

Fig. 1 Computational meshes of full-span flap model (left: baseline structured mesh, right: unstructured mesh, grid C).

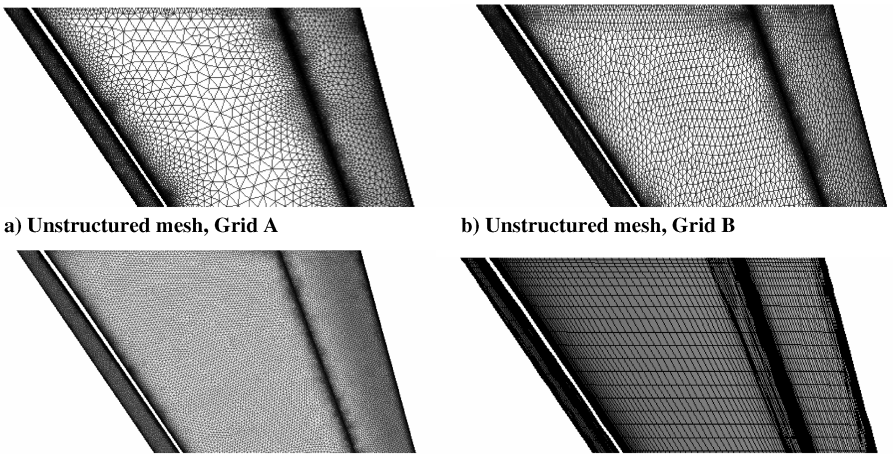

a) Unstructured mesh, Grid A b) Unstructured mesh, Grid B

c) Unstructured mesh, Grid C d) Baseline structured mesh

Fig. 2 Close-up view of surface meshes near the wing root of full-span flap model.

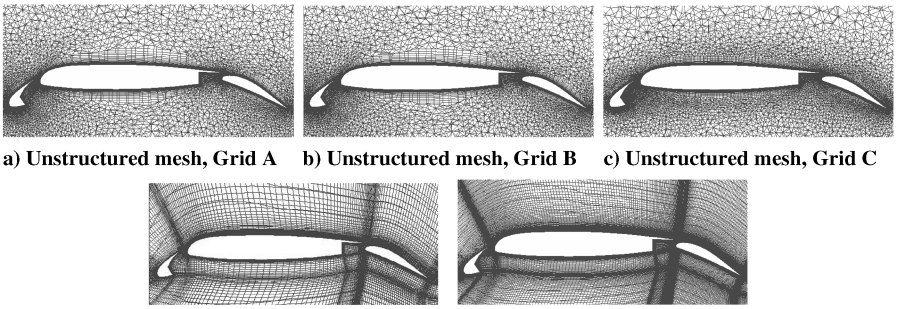

a) Unstructured mesh, Grid A b) Unstructured mesh, Grid B c) Unstructured mesh, Grid C

d) Baseline structured mesh e) Fine structured mesh

Fig. 3 Cross-sectional view of computational meshes at 50% span location.

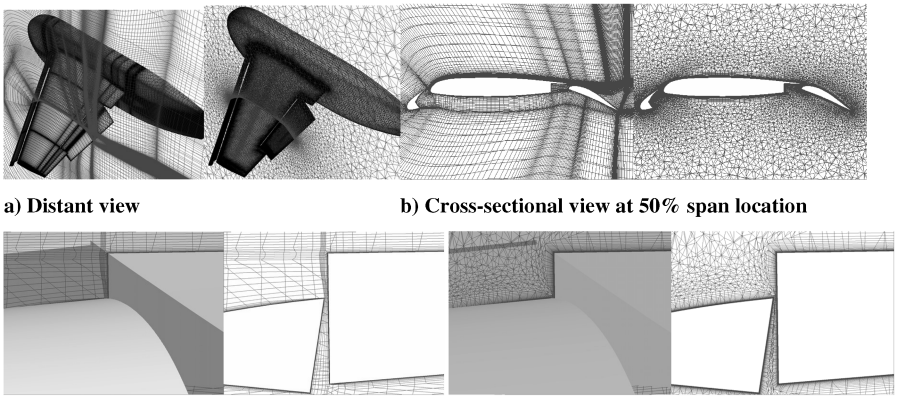

a) Distant view b) Cross-sectional view at 50% span location

c) Cross-sectional view near a gap between the main and flap wing

Fig. 4 Computational meshes of part-span flap model (left: baseline structured mesh, right: unstructured mesh).

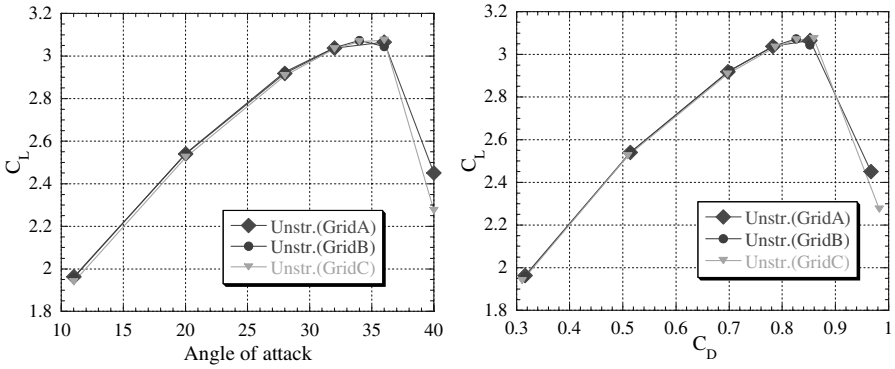

a) C_L-α b) C_L-C_D

Fig. 5 Comparison of C_L–α and C_L–C_D for unstructured meshes, grid A, grid B, and grid C (full-span flap model).

approximately 8.5 ft wide. The upper surface of the plate is 1.7 ft above the test section floor, which reduces the effective height of the test section to 9.6 ft for semispan testing [4].

For each configuration, multiblock structured meshes and unstructured meshes were generated. The multiblock structured meshes were generated with the commercial software, Gridgen. More than one month was required to generate a baseline mesh by an expert for each configuration. The unstructured meshes were generated with TAS-Mesh [21–24]. To generate the unstructured meshes from CAD data, only a few days were required.

For the full-span flap model, two multiblock structured meshes and three unstructured meshes were generated to investigate mesh dependency. For all meshes, the outer boundary is a semisphere whose radius is about $60c$. The baseline multiblock structured mesh shown in Fig. 1 has about 7.5×10^6 mesh points. The number of blocks is 586 blocks. The minimum spacing in the normal direction to the wing surface is $0.02/\sqrt{Re}$. A fine multiblock structured mesh that has about 8 times mesh points of the baseline multiblock structured mesh was also generated by adding mesh points in the i, j, and k direction, uniformly. The minimum spacing in the normal direction to the wing surface is $0.01/\sqrt{Re}$. The unstructured meshes have a different density of surface mesh. The surface meshes are shown in Fig. 2. The surface mesh of grid A shown in Fig. 2a was triangulated using nearly regular triangles and the regions near the center of the wing elements (slat, mother, and flap) that have low pressure derivatives were coarsened. The surface mesh of grid B was triangulated using stretched triangles that were stretched to a spanwise direction as shown in Fig. 2b. The stretching rate is about 1.25. The surface mesh of grid C was triangulated using nearly regular triangles and the regions near the center of the wing remain fine to increase the mesh resolution of the wake from the slat and mother as shown in Fig. 2c. The total numbers of the mesh points in the volume meshes are 1.08×10^6, 0.78×10^6, and 1.32×10^6, respectively. For all unstructured meshes, the minimum spacing in the normal direction to the wing surface is $0.01/\sqrt{Re}$. The cross-sectional views of the meshes at 50% span are shown in Fig. 3.

For the part-span flap model, two multiblock structured meshes and an unstructured mesh were generated. The baseline multiblock structured mesh shown in Fig. 4 has about 9.8×10^6 mesh points. The number of blocks is 848 blocks. The minimum spacing in the normal direction to the wing surface is $0.02/\sqrt{Re}$. A fine multiblock structured mesh that has about 8 times mesh points of the baseline multiblock structured mesh was also generated by adding mesh points in i, j, and k direction, uniformly. The minimum spacing in the normal direction to the wing surface is $0.01/\sqrt{Re}$. The unstructured mesh was generated using a strategy to generate the full-span flap mesh of grid A but the mesh resolution was further increased near the wing–fuselage junction and on the upper side of both slat and flap. The unstructured mesh has about 13×10^6 mesh points in volume mesh. The minimum spacing in the normal direction to the wing surface is $0.01/\sqrt{Re}$.

The unstructured surface meshing using isotropic triangles in this study [21,22] is semiautomatic and it took only a few hours. However, it requires a large number of mesh points at leading-edge and trailing-edge sections. The trailing edges of this model are blunt and very thin. To insert a sufficient number of mesh points using isotropic triangles, a huge number of mesh points are required. For both configurations, only one or two cells are placed in the trailing edges for the unstructured meshes as shown in Fig. 1b, compared with about 6 cells for the structured meshes.

In the current computations, M_∞ is 0.15 and the Re is 15×10^6. Fully turbulent flows are assumed in the computations.

IV. Results

A. Comparison of Results on Structured and Unstructured Mesh CFD Using the Same Turbulence Model

First, the results on structured and unstructured meshes using the same turbulence model, Spalart–Allmaras model, are compared.

1. *Full-Span Flap Model*

Figure 5 shows variations of C_L versus α and C_L versus C_D for computed results on each unstructured mesh. The differences between computations in C_L and C_D on grid A and grid B are only within 0.2 and 0.5%, respectively. The results on grid B using the moderate stretching of the surface triangular meshes did not get worse so much. The moderate stretching allows considerable saving of mesh points. Comparison of the results on grids B and C also shows good agreement. However, at angle of attack of 36 deg, which shows $C_{L\max}$, on grid C, the result on grid B shows a little lower lift and the stall. The difference is about 1%. Figure 6 shows the surface-restricted streamlines on each grid at $\alpha = 36$ deg. At the angle of attack, the flow began to separate at the outer side of the upper surface of the slat and the upper surface of the main wing near the wing tip. The flow separation on the slat was very sensitive to the mesh density. The result on grid B shows larger flow separation on the outer side of the upper surface of the slat and the backward region on the main wing. These flow separations cause the decrease of C_L at this angle of attack on grid B.

Figure 7 shows C_L–α and C_L–C_D for computed results on two structured meshes and an unstructured mesh, grid C, and experimental data [4].** Uncorrected and corrected experimental data are also shown in Fig. 7. In the published date at the Web site,†† the corrected experimental data near the stall angle of attack are not available. As for C_L–α, although all computational results predict slightly higher C_L (about 1%), the results show good agreement with the experimental data at the moderate angles of attack. The difference between computations in C_L at the moderate angles of attack is 1.0% and the difference in $C_{L\max}$ is 1.4%, which is considered reasonable. Considering the tendency of the wall-interference correction from the uncorrected experimental data, a stall delay of 2–4 deg may be

**See http://db-www.larc.nasa.gov/trapwing/archive/register [cited 30 December 2005].

††See http://db-www.larc.nasa.gov/trapwing/archive/register [cited 30 December 2005].

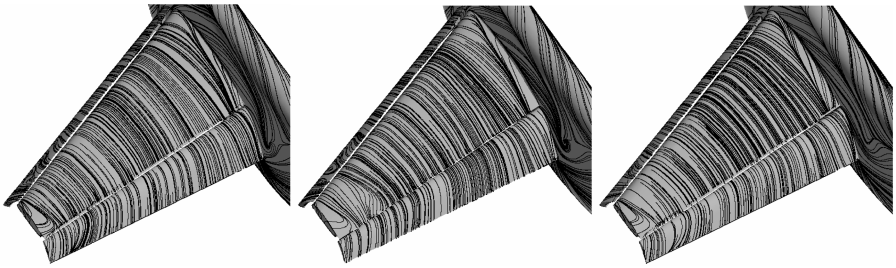

a) Unstructured mesh, Grid A b) Unstructured mesh, Grid B c) Unstructured mesh, Grid C

Fig. 6 Surface-restricted stream lines at $\alpha = 36.00$ deg (full-span flap model, SA turbulence model).

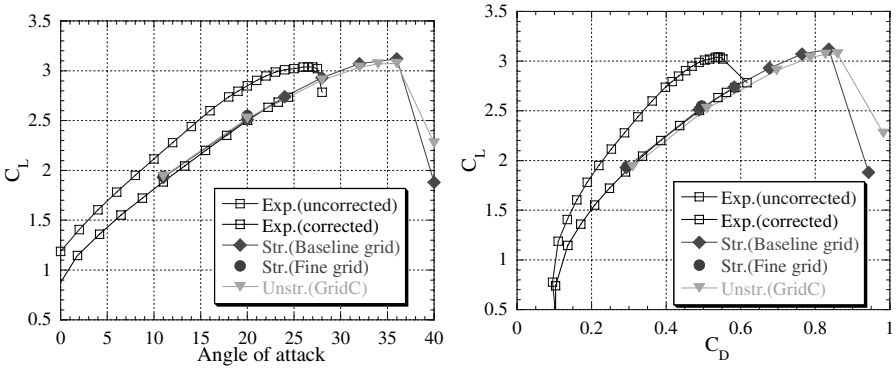

a) C_L-α b) C_L-C_D

Fig. 7 Comparison of C_L–α and C_L–C_D between experimental results and computational results (full-span flap model).

observed in our computations. As for C_L–C_D, the overall level and the tendency of all computational results agree well with the wind-tunnel results. However, differences between computations in C_D are relatively larger. The differences between the results on the baseline structured mesh and the unstructured mesh are about 200–300 drag counts, which is about 3–6% of the C_D.

Figure 8 shows the span load distribution at an angle of attack of 20.02 deg. For the full-span flap model, the span load distribution is close to being elliptical. In Fig. 9, $C_{D\text{profile estimated}}$ are compared. The value is obtained by subtracting the estimated induced drag, $C_L^2/\pi/AR/e$, from C_D. Here, e was estimated to be roughly 0.95 by a simplified method using the following relationship: $C_D = C_{D\min} + C_L^2/\pi/AR/e$. The estimated induced drag can be more than 85% of the total drag. The difference in $C_{D\text{profile estimated}}$ between results on all unstructured meshes is small. In the three-dimensional high-lift case, the induced drag is so large that the difference in C_D between structured and unstructured meshes seems smaller. Comparing the computational results in Fig. 9, however, the estimated $C_{D\text{profile estimated}}$ for unstructured mesh is much higher.

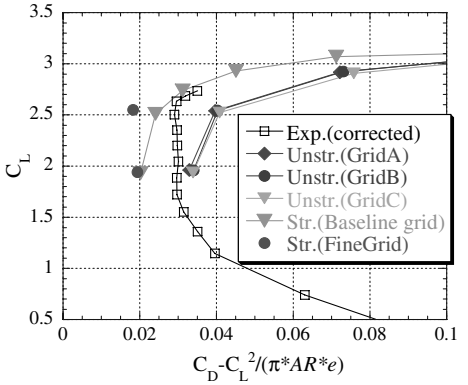

Fig. 9 Comparison of C_L–$C_{D\text{profile estimated}}$ between experimental results and computational results (full-span flap model).

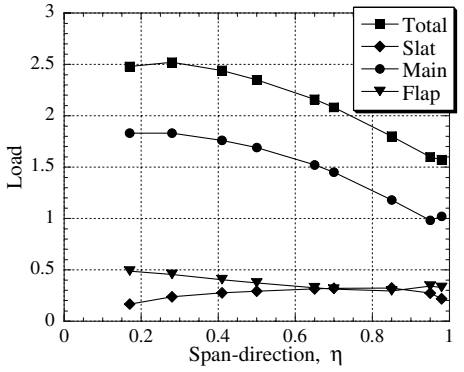

Fig. 8 Span load distribution of full-span flap model at $\alpha = 20.02$ deg (baseline structured mesh).

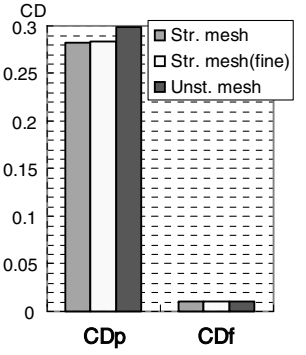

Fig. 10 Comparison of drag components between computational results on structured and unstructured meshes at $\alpha = 16.70$ deg (full-span flap model).

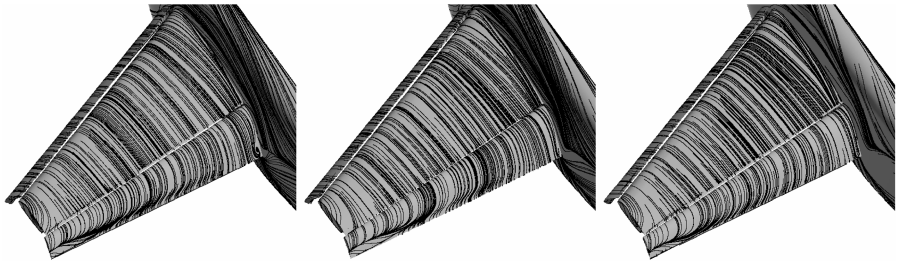

a) Unstructured mesh, Grid A b) Unstructured mesh, Grid B c) Unstructured mesh, Grid C

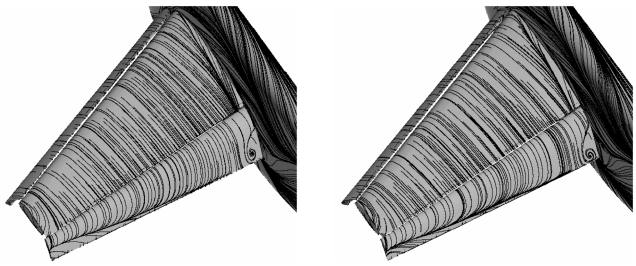

d) Baseline structured mesh e) Fine unstructured mesh

Fig. 11 Surface-restricted stream lines at $\alpha = 20.18$ deg (full-span flap model, SA turbulence model).

In Fig. 10, C_D at angle of attack of 11.02 deg is broken down into C_{Dp} and C_{Df}. The results on fine structured mesh are also shown here. The percentage of pressure drag is more than 95% in the total drag. The difference between the baseline and fine structured meshes in C_{Dp} and C_{Df} is only 20 drag counts and 2 drag counts, respectively. The differences between the unstructured mesh, grid C, and the fine structured mesh in C_{Dp} and C_{Df} is about 150 drag counts ($\approx$4%) and 5 drag counts ($\approx$5%), respectively.

Figures 6 and 11–13 show the surface-restricted streamlines at angles of attack of 20.18, 36, and 40 deg. Overall flow patterns are similar but difference can be seen in the corner flow near the wing–fuselage junction. In this configuration, there is no fairing at the junction. Flow separation can be observed at this corner. Especially at angle of attack of 20.18 deg, a considerable difference can be seen in the corner flow near the flap–fuselage junction by the mesh in Fig. 11. On the structured meshes, larger separation can be seen in the region than that on the unstructured meshes. At a higher angle of attack of 36 deg where the computational results show $C_{L\max}$, relatively larger separation appears near the junction of the main wing and the separation near the junction of the flap wing disappears, as shown in Figs. 6 and 12. At an angle of attack of 40 deg after the stall as shown in Fig. 13, both computational results on structured and unstructured meshes show similar stall pattern that the flow separates from the outer side of the upper surface of the slat largely although the computational results were not converged any longer.

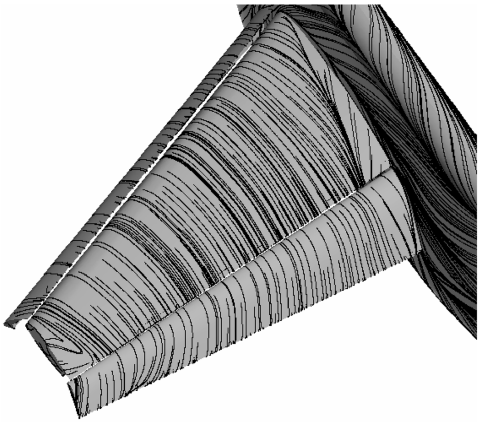

Fig. 12 Surface-restricted stream lines at $\alpha = 36.00$ deg on baseline structured mesh (full-span flap model, SA turbulence model).

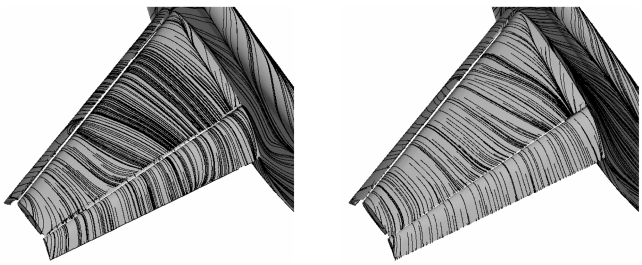

a) Unstructured mesh, Grid C b) Baseline structured mesh

Fig. 13 Surface-restricted stream lines at $\alpha = 40.00$ deg (full-span flap model, SA turbulence model).

Figure 14 shows the close-up view of the surface-restricted streamlines at an angle of attack of 20.18 deg and the surface meshes. As for the results on the unstructured meshes, the result on grid A, which has relatively lower mesh resolution near the junction, shows larger separation near the flap–fuselage junction. As for the results on the structured meshes, the large separation near the flap–fuselage junction can be seen even on the fine structured mesh where the mesh resolution is doubled in all directions as shown in Figs. 14d and 14e. Figure 14f shows the result on a structured mesh where the mesh resolution near the junction is enhanced 4 times only in the spanwise direction. As a result, the size of the flow separation becomes smaller and the similarity with the result of unstructured mesh of grid C is improved. Especially on structured meshes, stretched elements in the spanwise direction are generally used. The flow separation is very sensitive to mesh resolution especially in the spanwise direction. By refining the mesh, 1% changes in C_L and C_D are also obtained. This emphasizes the importance in the mesh resolution and quantitative prediction of the flow separation at such corner.

2. *Part-Span Flap Model*

Figure 15 shows C_L–α and C_L–C_D for computed results on two structured meshes and an unstructured mesh, and uncorrected and corrected experimental data.[‡‡] As for C_L–α, all computational results show good agreement with the experimental data at the moderate angles of attack. The difference is about 1.5–3%. All computational

[‡‡]See http://db-www.larc.nasa.gov/trapwing/archive/register [cited 30 December 2005].

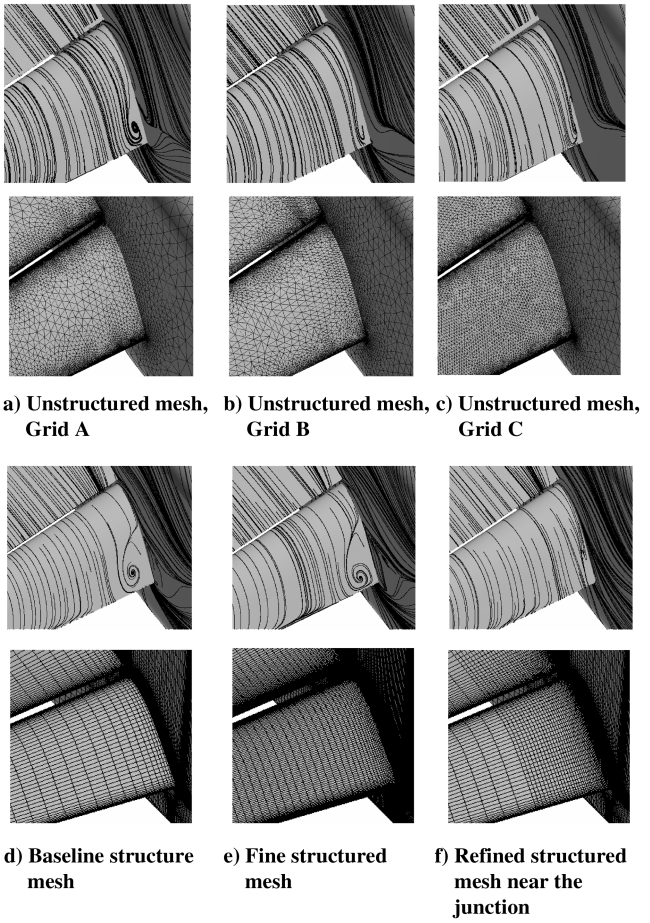

a) Unstructured mesh, Grid A | b) Unstructured mesh, Grid B | c) Unstructured mesh, Grid C

d) Baseline structure mesh | e) Fine structured mesh | f) Refined structured mesh near the junction

Fig. 14 Close-up view of surface-restricted stream lines at $\alpha = 20.18$ deg and the surface meshes (full-span flap model, SA turbulence model).

results predict slightly higher C_L than experimental results, which is the same tendency as the results on the full-span flap model. As in the case of the computations of full-span flap model, a slight delay of stall angle of attack may be observed in our computations considering the tendency of the wall-interference correction from the uncorrected experimental data. The differences between computations by the baseline structured and unstructured meshes in C_L at the moderate angles of attack are about 1%, which is considered acceptable. However, at higher angles of attack (≥ 30 deg), the difference between computations by the baseline structured and unstructured meshes becomes larger. The result on the baseline structured mesh shows lower C_L. On the other hand, C_L predicted by finer structured mesh is slightly higher than those by the baseline structured mesh and closer to C_L by the unstructured mesh ($\leq 1\%$). The reduction of C_L by the change of the geometry from the full-span flap to the part-span flap can be well predicted.

Figures 16–19 show the surface-restricted streamlines at angles of attack of 22.33, 35, 40, and 45 deg. At an angle of attack of 22.33 deg, all computational results in Fig. 16 show the similarity of the surface flow, although a little difference can be found in the separated region near the wing–fuselage junction. At an angle of attack of 35 deg where the result on the baseline structured mesh begins to show lower C_L than other results, the separated region on the baseline structured mesh near the wing–fuselage junction increases as shown in Fig. 17. At a higher angle of attack of 40 deg where the computational results on the baseline structured and unstructured meshes show $C_{L\max}$ in Fig. 18, the separated region on the baseline structured mesh increases more. On the other hand, the results on the fine structured mesh show the similarity regarding the separation with the results of unstructured mesh. As discussed in the case of the full-span flap model, it seems that this excessive flow separation results from the insufficient mesh resolution. This excessive flow separation causes the reduction of C_L and it results in the difference with the fine structured and unstructured mesh results. At an angle of attack of 40 deg, the result on the fine structured mesh shows earlier stall than other results. The flow separates from the outer side of the slat and main wing on the fine structured mesh, although the flow over the main wing remains attached on the other results. At an angle of attack of 45 deg after the stall shown in Fig. 19, the computational results were not converged and the size of the separation was fluctuant. At this high angle of attack, it is possible that there is no steady state solution. However, it is found that both computational results on structured and unstructured meshes show similar stall pattern. As in the case of the computations of full-span flap model, the quantitative prediction of the local flow separation near the wing–fuselage junction is one of the important issues to improve the accuracy of computational results.

As for C_L–C_D shown in Fig. 15b, the overall level and the tendency of all computational results agree well with the wind-tunnel results. The differences between computations by the baseline structured and unstructured meshes in C_D are about 100–200 drag counts, which is about 5%. Figure 20 shows the span load distribution at an angle of attack of 16.70 deg. For the part-span flap model, the span load distribution is not very close to being elliptical due to the effect by part-span flap. In Fig. 21, $C_{D\text{profile estimated}}$ are compared. Here, e was estimated to be roughly 0.95 by a simplified method, again. Comparing the computational results in Fig. 21, it is found that the results on the unstructured mesh show better agreement with experimental data. However, the estimated $C_{D\text{profile estimated}}$ by fine structured mesh is much lower than that by the baseline structured mesh. It is the same tendency with the previous full-span flap case. In addition, spurious drag generally decreases on finer meshes by the reduction of the numerical error. Thus, these facts show that the results by unstructured mesh predict higher drag, numerically. Improvement of the drag prediction for high-lift flows is one of the important issues to resolve.

B. Comparison of Turbulence Models in an Unstructured Mesh Code

Next, the difference of flows by turbulence models is evaluated using an unstructured mesh CFD code, TAS code. In this study, two kinds of turbulence models explained in Sec. II were used: SA with a modification to reduce the eddy viscosity in the regions of high vorticity and Menter's SST k–ω model.

1. *Full-Span Flap Model*

The comparisons were performed on grid A. Figure 22 shows C_L–α and C_L–C_D as a function of the turbulence model. The difference in C_L is at most 0.5% by the turbulence model and the slope of C_L is almost the same with each other at moderate angles of attack. The stall angle and maximum lift $C_{L\max}$ by the SST model are lower than those by the SA model and it shows better agreement with experimental results in this case considering the tendency of the wall-interference correction from the uncorrected experimental data. The differences in $C_{L\max}$ and the stall angle are 2.2% and 3–4 deg by the turbulence model. The SA model produces relatively larger eddy viscosity and it may be responsible for the delay in stall. Regarding C_L–C_D, both models produce similarly in characteristic curvature to experimental data. The difference in C_D at a constant C_L is about 1%. In Fig. 23, $C_{D\text{profile estimated}}$ are compared. The difference in $C_{D\text{profile estimated}}$ is also small. Figure 24 shows the drag components divided into C_{Dp} and C_{Df}. The difference in C_{Dp} is 1% at most. On the other hand, C_{Df} shows larger difference, which is about 5–10 drag count ($\leq 10\%$).

Figures 25 and 26 show comparisons of C_P and C_f distribution on the midspan of the wing at $\alpha = 20.18$ deg. The difference in C_P is small. On the other hand, the results by the SST model show lower C_f near the leading edge of each wing element. The growth of the eddy viscosity from the leading edge by the SST model tends to be slower than that by the present SA model. This delay leads to lower C_f by the SST model.

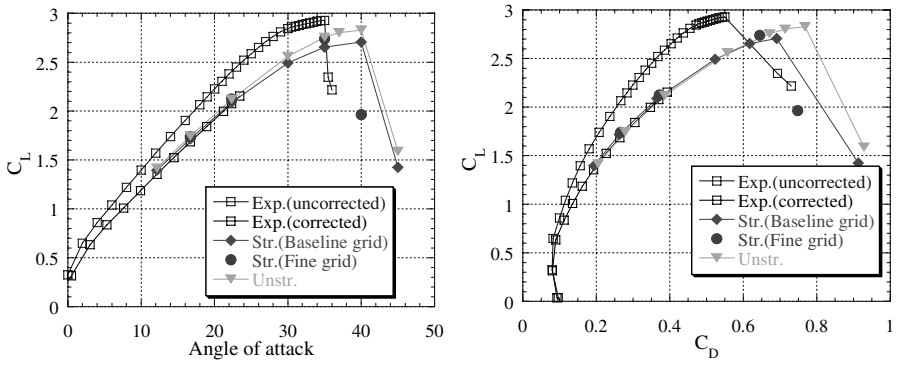

a) C_L-α **b) C_L-C_D**

Fig. 15 Comparison of C_L–α and C_L–C_D between experimental results and computational results (part-span flap model).

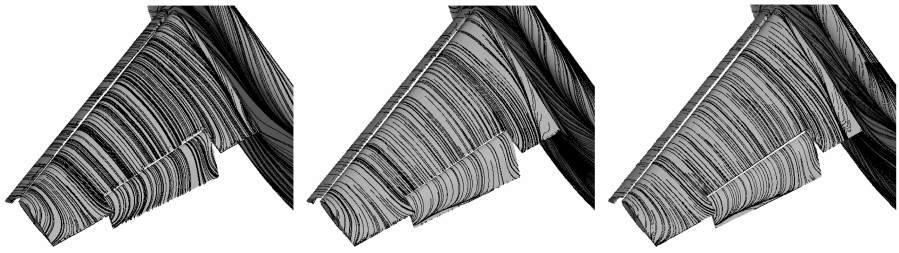

a) Unstructured mesh **b) Baseline structured mesh** **c) Fine structured mesh**

Fig. 16 Surface-restricted stream lines at $\alpha = 22.33$ deg (part-span flap model, SA turbulence model).

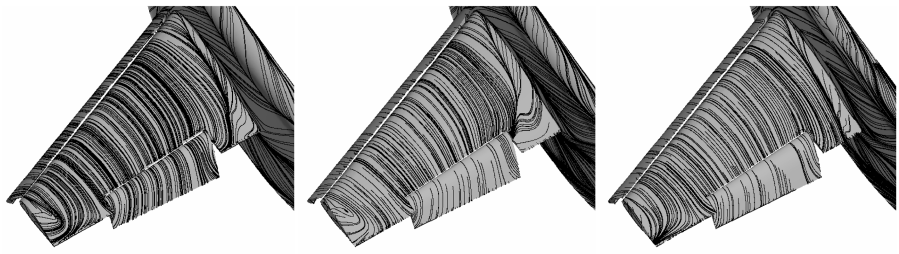

a) Unstructured mesh **b) Baseline structured mesh** **c) Fine structured mesh**

Fig. 17 Surface-restricted stream lines at $\alpha = 35.00$ deg (part-span flap model, SA turbulence model).

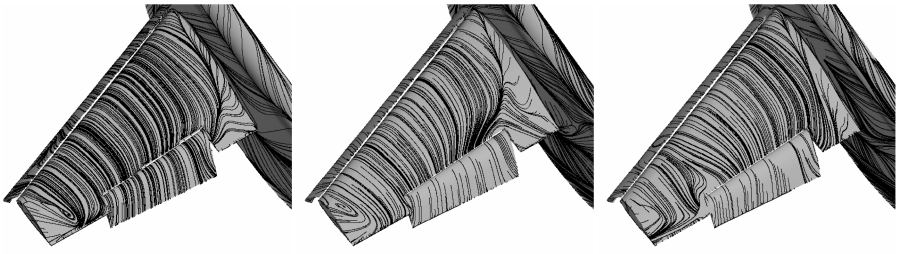

a) Unstructured mesh **b) Baseline structured mesh** **c) Fine structured mesh**

Fig. 18 Surface-restricted stream lines at $\alpha = 40.00$ deg (part-span flap model, SA turbulence model).

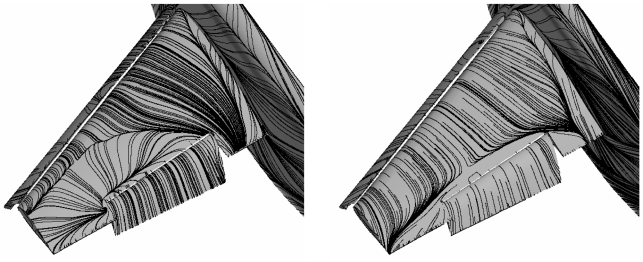

a) Unstructured mesh **b) Baseline structured mesh**

Fig. 19 Surface-restricted stream lines at $\alpha = 45.00$ deg (part-span flap model, SA turbulence model).

Figures 27–29 show the surface-restricted streamlines of the computational results using the SST model at $\alpha = 20.18$, 32, and 34 deg and Fig. 30 shows the results using the SA model at $\alpha = 32$ deg. Compared with Figs. 11 and 27, the difference of the overall flow pattern by the turbulence models is small at $\alpha = 20.18$ deg. At an angle of attack of 32 deg where the computational result by the SST model shows $C_{L\max}$, the flow separation on the upper surface of the main wing near the wing tip appears, although it cannot be seen in the results by the SA model at this angle of attack. At angle of attack of 34 deg in Fig. 29, the flow starts to separate from the outer side of the upper surface of the slat. In these computations, both computational results by the SA and SST

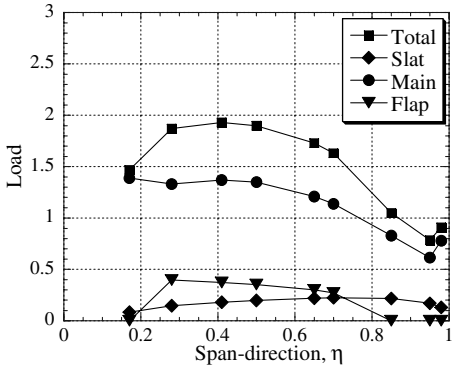

Fig. 20 Span load distribution of part-span flap model at $\alpha = 16.70$ deg (baseline structured mesh).

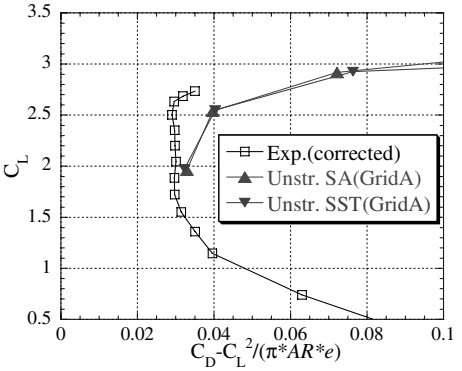

Fig. 23 Comparison of C_L–$C_{D\text{profile estimated}}$ between experimental results and computational results (full-span flap model).

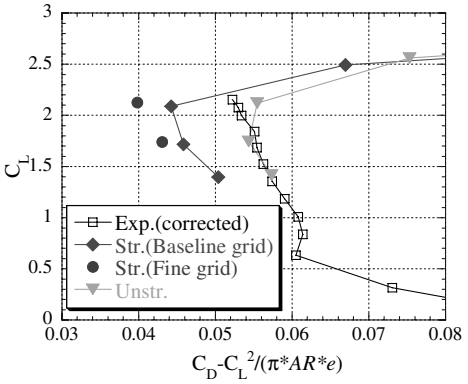

Fig. 21 Comparison of C_L–$C_{D\text{profile estimated}}$ between experimental results and computational results (part-span flap model).

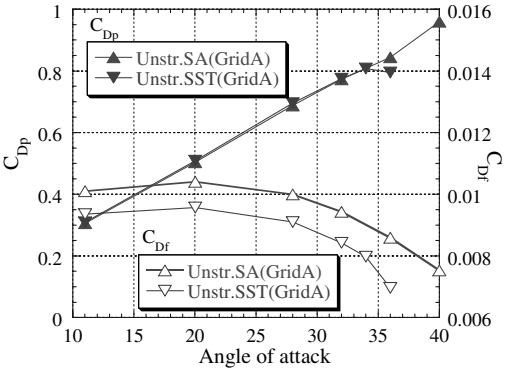

Fig. 24 Comparison of pressure drag C_{Dp} and friction drag C_{Df} (full-span flap model).

models can produce a similar stall pattern although the stall angle is different.

2. Part-Span Flap Model

Figures 31 and 32 show C_L–α, C_L–C_D, C_{Dp}–α, and C_{Df}–α. As in the case of the full-span flap model, the differences in C_L, C_D, and C_{Dp} are considerably smaller at moderate angles of attack and the stall angle and $C_{L\max}$ by the SST model are lower than those by the SA model. The difference in C_L is at most 0.7% and the average is 0.3% by turbulence model at moderate angles of attack. The differences in $C_{L\max}$ and the stall angle are 1.6% and 3 deg. The difference in C_{Df} is about 5 drag count ($\leq 6\%$).

Figures 33–35 show the surface-restricted streamlines of the computational results using the SST model at $\alpha = 22.33$, 37, and 40 deg and Fig. 36 shows the results using the SA model at $\alpha = 37$ deg. Compared with Figs. 16, 33, 34, and 36, the difference of the overall flow pattern by the turbulence models is small before the computational result by the SST model shows the stall. At the angle of attack of 40 deg, the computational result by the SST model shows the flow separation from the outer side of the upper surface of the slat. Although the stall angle is different, the stall pattern is not different by SA and SST models even on the part-span flap model.

Figures 37 and 38 show the entropy contours at 50% span location. In the cove of the slat, the level of the entropy is different by the turbulence models. However, the wake flow is not largely changed by the turbulence models. In the present three-dimensional computations, at these moderate angles of attack, SA and SST models can produce similar aerodynamic forces as is discussed in our previous study for two-dimensional computations [8,9]. At higher angles of attack near the stall, the SST model gives better results in the present cases. However, because the SA model is a one-equation model and the SST model is a two-equation model, the SST model requires larger computational cost compared with the SA model. In

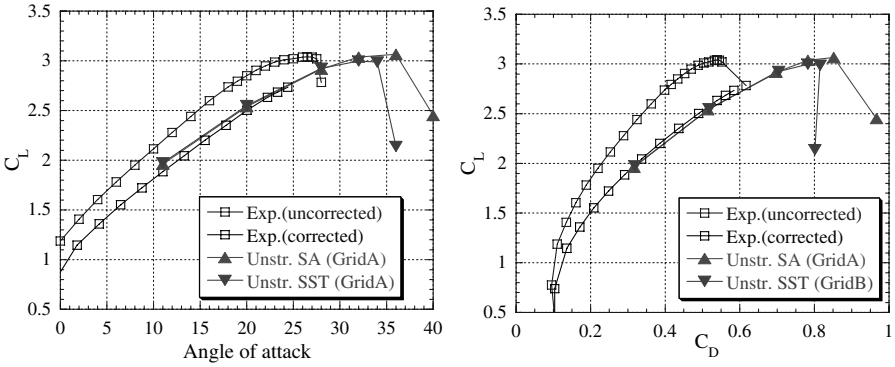

a) C_L-α **b) C_L-C_D**

Fig. 22 Comparison between experimental results and computational results (full-span flap model).

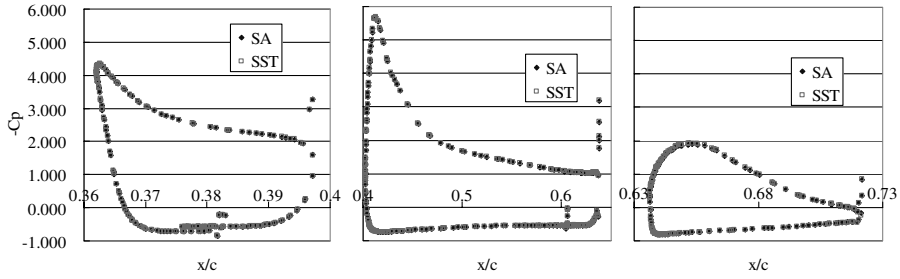

a) Slat b) Main wing c) Flap

Fig. 25 Comparison of C_P at $\alpha = 20.18$ deg at 50% span location of full-span flap model.

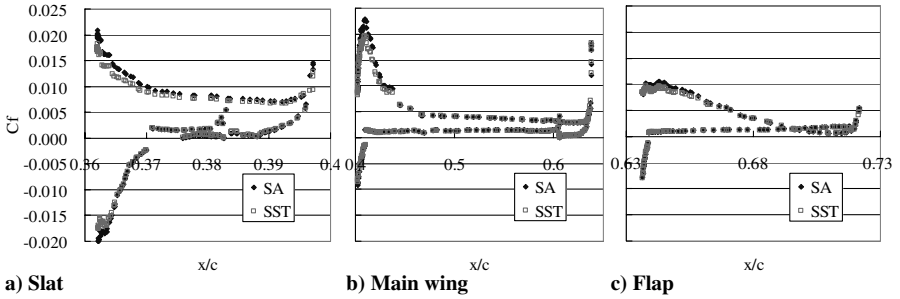

a) Slat b) Main wing c) Flap

Fig. 26 Comparison of C_f at $\alpha = 20.18$ deg at 50% span location of full-span flap model.

the present computations, the SA model was also superior with regard to convergency and stability. The SST model required longer CPU time to get converged results compared with the SA model. This study shows that the predicted values of the maximum lift and the angle at which the stall occurred were very sensitive to turbulence model. Practical use requires understanding of the characteristics of each turbulence model when it is applied to this kind of flow and careful use depending on the problems.

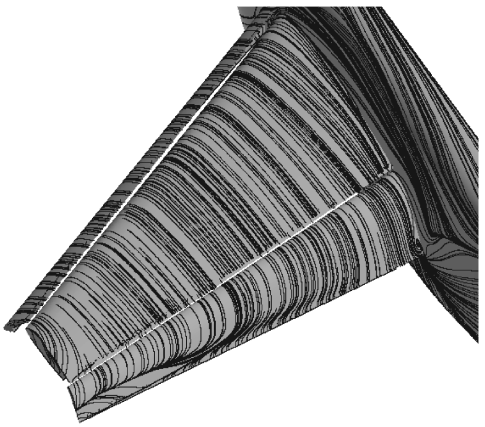

Fig. 27 Surface-restricted stream lines at $\alpha = 20.18$ deg (full-span flap model, SST turbulence model).

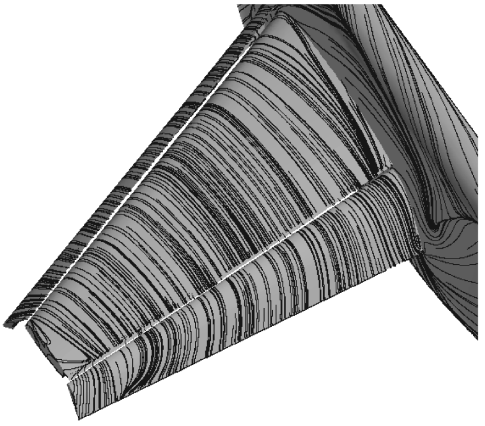

Fig. 28 Surface-restricted stream lines at $\alpha = 32.00$ deg (full-span flap model, SST turbulence model).

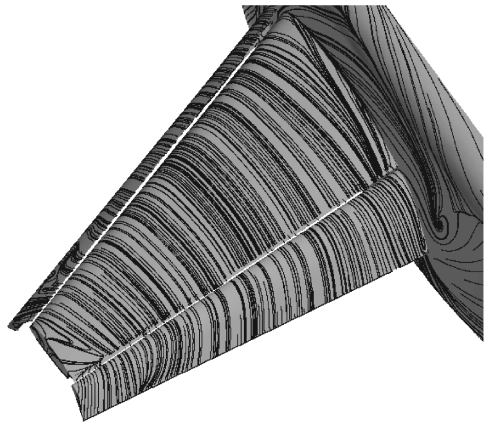

Fig. 29 Surface-restricted stream lines at $\alpha = 34.00$ deg (full-span flap model, SST turbulence model).

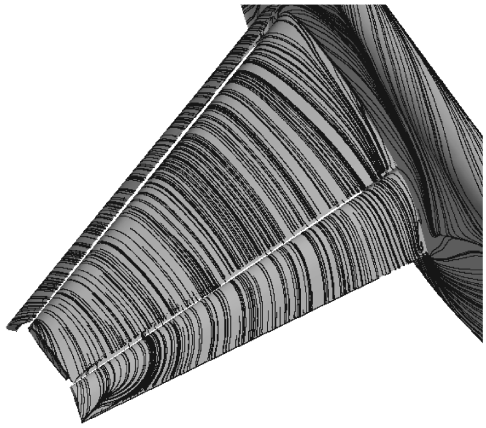

Fig. 30 Surface-restricted stream lines at $\alpha = 32.00$ deg (full-span flap model, SA turbulence model).

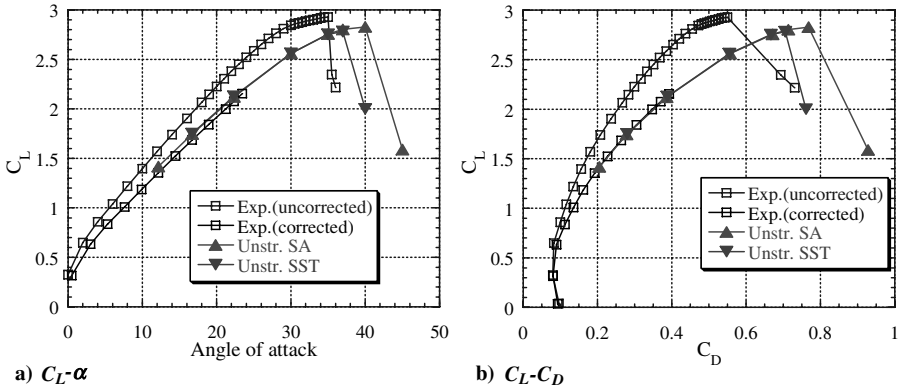

a) C_L-α b) C_L-C_D

Fig. 31 Comparison between experimental results and computational results (part-span flap model).

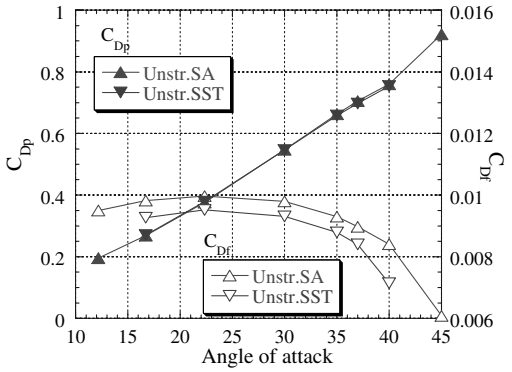

Fig. 32 Comparison of pressure drag C_{Dp} and friction drag C_{Df} (part-span flap model).

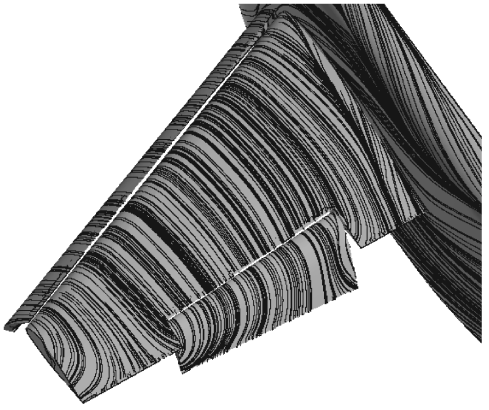

Fig. 33 Surface-restricted stream lines at $\alpha = 22.33$ deg (part-span flap model, SST turbulence model).

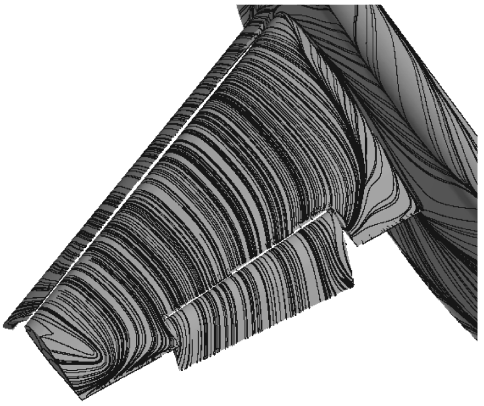

Fig. 34 Surface-restricted stream lines at $\alpha = 37.00$ deg (part-span flap model, SST turbulence model).

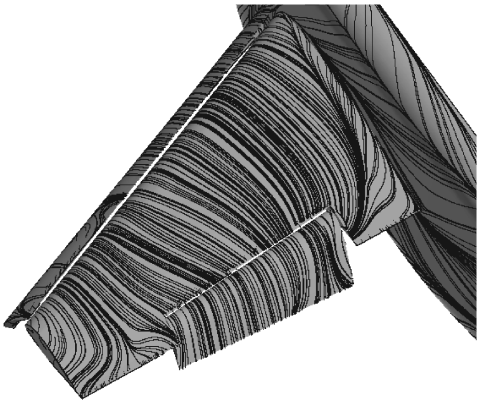

Fig. 35 Surface-restricted stream lines at $\alpha = 40.00$ deg (part-span flap model, SST turbulence model).

V. Conclusions

To improve the reliability of aerodynamic force prediction in the flow simulation around high-lift devices on multiblock structured and unstructured mesh, computations of two kinds of three-element trapezoidal wings with full-span flap or part-span flap have been performed. Studies of the mesh dependencies and the effect of the turbulence models have been performed.

In both configurations, the mesh resolution near the wing–fuselage junction was important in improving the accuracy of computational results. Excessive flow separation in the corner flow near the wing–fuselage junction resulted from the insufficient mesh resolution especially in a spanwise direction. It mainly caused the difference in C_L between the computations. As for the stall prediction, both computational results on structured and unstructured meshes predicted the similar stall pattern. The differences in $C_{L\,\max}$ and the stall angle were acceptable. As for C_D, it was shown that the

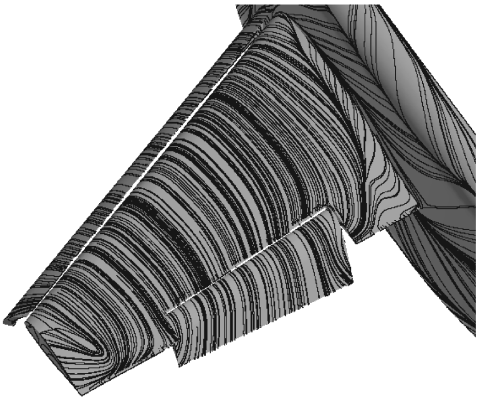

Fig. 36 Surface-restricted stream lines at $\alpha = 37.00$ deg (part-span flap model, SA turbulence model).

a) SA model

b) SST model

Fig. 37 Entropy contours at 50% span location at $\alpha = 16.70$ deg of part-span flap model.

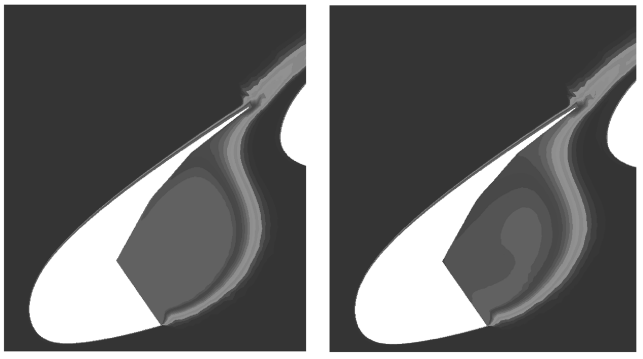

a) SA model b) SST model

Fig. 38 Close-up view of entropy contours near the slat at 50% span location at $\alpha = 16.70$ deg.

results on unstructured mesh predicted higher drag numerically by the detailed comparison of computational results and it is one of the issues to resolve. Thus, to validate and develop CFD methods, detailed comparison of computational results from several CFD codes and mesh topologies is helpful.

The difference of aerodynamic forces by the turbulence model was considerably smaller before stall although the results by the SST model showed lower C_f near the leading edge of each wing element by the slower growth of the eddy viscosity. The stall angle and maximum lift $C_{L\max}$ by the SST model were lower than those by the SA model, although the stall patterns were similar. It showed better agreement with experimental results in the present cases. This study shows that the predicted values of the maximum lift and the angle at which the stall occurred were very sensitive to the turbulence model. Practical use requires an understanding of the characteristics of each turbulence model when it is applied to this kind of flow.

References

[1] Meredith, P. T., "Viscous Phenomena Affecting High-Lift Systems and Suggestions for Future CFD Development," *High-Lift Systems Aerodynamics*, CP-515, AGARD, Sept. 1993, pp. 19-1–19-8.

[2] Rumsey, C. L., and Ying, S. X., "Prediction of High Lift: Review of Present CFD Capability," *Progress in Aerospace Sciences*, Vol. 38, No. 2, 2002, pp. 145–180.

[3] Hansen, H., Thiede, P., Moens, F., Rudnik, R., and Quest, J., "Overview About the European High Lift Research Programme EUROLIFT," AIAA Paper 2004-0767, Jan. 2004.

[4] Johnson, P., Jones, K. M., and Madson, M., "Experimental Investigation of a Simplified 3-D High Lift Configuration in Support of CFD Validation," AIAA Paper 2000-4217, Aug. 2000.

[5] Nash, S. M., and Rogers, S. E., "Numerical Study of a Trapezoidal Wing High-Lift Configuration," SAE Paper 1999-01-5559, Oct. 1999.

[6] Rogers, S. E., Roth, K., and Nash, S. M., "CFD Validation of High-Lift Flows with Significant Wind-Tunnel Effects," AIAA Paper 2000-4218, Aug. 2000.

[7] Chaffin, S. M., and Pirzadeh, S., "Unstructured Navier–Stokes High-Lift Computations on a Trapezoidal Wing," AIAA Paper 2005-5084, June. 2005.

[8] Lei, Z., Murayama, M., Takenaka, K., and Yamamoto, K., "CFD Validation for High-Lift Devices: Two-Element Airfoil," *Transactions of the Japan Society for Aeronautical and Space Sciences*, Vol. 49, No. 163, 2006, pp. 31–39.

[9] Murayama, M., Lei, Z., Mukai, J., and Yamamoto, K., "CFD Validation for High-Lift Devices: Three-Element Airfoil," *Transactions of the Japan Society for Aeronautical and Space Sciences*, Vol. 49, No. 163, 2006, pp. 40–48.

[10] Murayama, M., Yamamoto, K., and Kobayashi, K., "Validation of Flows on High-Lift Configurations by the Structured- and Unstructured-Mesh Method," AIAA Paper 2005-1226, Jan. 2005.

[11] Murayama, M., Nakahashi, K., and Matsushima, K., "A Robust Method for Unstructured Volume/Surface Mesh Movement," *Transactions of the Japan Society for Aeronautical and Space Sciences*, Vol. 46, No. 152, Aug. 2003, pp. 104–112.

[12] Murayama, M., Nakahashi, K., and Sawada, K., "Simulation of Vortex Breakdown Using Adaptive Grid Refinement with Vortex–Center Identification," *AIAA Journal*, Vol. 39, No. 7, July 2001, pp. 1305–1312.

[13] Spalart, P. R., and Allmaras, S. R., "A One-Equation Turbulence Model for Aerodynamic Flows," AIAA Paper 92-0439, Jan. 1992.

[14] Menter, F. R., "Zonal Two Equation k–ω Turbulence Models for Aerodynamic Flows," AIAA Paper 93-2906, July 1993.

[15] Kusunose, K., and Cao, H., "Prediction of Transition Location for a 2-D Navier–Stokes Solver for Multi-Element Airfoil Configurations," AIAA Paper 94-2376, June 1994.

[16] Krumbein, A., "Automatic Transition Prediction and Application to High Lift Multi-Element Configurations," AIAA Paper 2004-2543, June 2004.

[17] Takaki, R., Yamamoto, K., Yamane, T., Enomoto, S., and Mukai, J., "The Development of the UPACS CFD Environment," *High Performance Computing: Proceedings of the International Symposium on High Performance Computing 2003*, Springer, Tokyo, Japan, 2003, pp. 307–319.

[18] Yamamoto, K., Ochi, A., Shima, E., and Takaki, R., "CFD Sensitivity of Drag Prediction on DLR-F6 Configuration by Structured Method and Unstructured Method," AIAA Paper 2004-0398, Jan. 2004.

[19] Shima, E., "A Simple Implicit Scheme for Structured/Unstructured CFD," *Proceedings of the 29th Fluid Dynamics Symposium*, 1997, pp. 325–328.

[20] Nakahashi, K., Togashi, F., Fujita, T., and Ito, Y., "Numerical Simulations on Separation of Scaled Supersonic Experimental Airplane from Rocket Booster at Supersonic Speed," AIAA Paper 2002-2843, June 2002.

[21] Ito, Y., and Nakahashi, K., "Direct Surface Triangulation Using Stereolithography Data," *AIAA Journal*, Vol. 40, No. 3, March 2002, pp. 490–496.

[22] Ito, Y., and Nakahashi, K., "Surface Triangulation for Polygonal Models Based on CAD Data," *International Journal for Numerical Methods in Fluids*, Vol. 39, No. 1, 2002, pp. 75–96.

[23] Sharov, D., and Nakahashi, K., "A Boundary Recovery Algorithm for Delaunay Tetrahedral Meshing," *Proceedings of 5th International Conference on Numerical Grid Generation in Computational Field Simulations*, 1996, pp. 229–238.

[24] Ito, Y., and Nakahashi, K., "Improvements in the Reliability and Quality of Unstructured Hybrid Mesh Generation," *International Journal for Numerical Methods in Fluids*, Vol. 45, No. 1, May 2004, pp. 79–108.

[25] Obayashi, S., and Guruswamy, G. P., "Convergence Acceleration of an Aeroelastic Navier–Stokes Solver," *AIAA Journal*, Vol. 33, No. 6, 1995, pp. 1134–1141.

[26] Sharov, D., and Nakahashi, K., "Reordering of Hybrid Unstructured Grids for Lower-Upper Symmetric Gauss–Seidel Computations," *AIAA Journal*, Vol. 36, No. 3, 1998, pp. 484–486.

[27] Dacles-Mariani, J., Zilliac, G. G., Chow, J. S., and Bradshaw, P., "Numerical/Experimental Study of a Wingtip Vortex in the Near Field," *AIAA Journal*, Vol. 33, No. 9, 1995, pp. 1561–1568.

[28] Lei, Z., "Effect of RANS Turbulence Models on Computational of Separated Flows over a Wing-Body Configuration," *Transactions of the Japan Society for Aeronautical and Space Sciences*, Vol. 48, Nov. 2005, pp. 150–160.

[29] Matsuo, Y., Nakamura, T., Tsuchiya, M., Ishizuka, T., Fujita, N., Ohkawa, H., Hirabayashi, Y., Takaki, R., Yoshida, M., Nakamura, K., Yamamoto, K., Suematsu, K., and Iwamiya, T., "Numerical Simulator 3: Building a Terascale Distributed Parallel Computing Environment for Aerospace Science and Engineering," *Proceedings of the Parallel Computational Fluid Dynamics 2002 Conference*, Elsevier Science, B. V., Nara, Japan, 2003, pp. 187–194.